Electrochimica Acta 464 (2023) 142935

Contents lists available at ScienceDirect

Electrochimica Acta

journal homepage: www.journals.elsevier.com/electrochimica-acta

Vanquishing CZTSSe deep defects to enhance photoelectrocatalytic water splitting

Mileny dos Santos Araujo, Hugo Leandro Sousa dos Santos, Marina Medina, Arthur Corrado Salomao, Lucia Helena Mascaro *, Marcos Antonio Santana Andrade Junior

Federal University of São Carlos, Chemistry Department, Washington Luiz Highway, km 235, São Carlos, SP 13565-905, Brazil

A R T I C L E I N F O

Keywords:
Bulk defects
Band tailing
Chalcogenides
Water splitting
Silver

A B S T R A C T

$Cu_2ZnSn(S,Se)_4$ (CZTSSe) is a promising material as a photocathode for photoelectrochemical (PEC) water splitting because it is inexpensive and composed of earth-abundant elements. However, it has a high density of deep defects, such as Cu_{Zn} and Zn_{Cu} antisites, which is pointed out as the main cause of band tailing and low onset potential-based PEC devices. By substituting 10% of Cu^+ by Ag^+, the onset potential shifts positively from 0.2 to 0.4 V_{RHE}, the photocurrent is almost three-folded, and solar-to-hydrogen efficiency is 6 times higher than that for the Ag-free photocathode. Absolute intensity photoluminescence (AIPL) in different light intensities was used to demonstrate that the Ag-substitution vanquishes the Cu/Zn-related defects. The quasi-Fermi level splitting (QFLS) values are obtained fitting the Katahara-modified model of the Planck Law, and the curve QFLS *versus* light intensity provides the quasi-Fermi Level pinning. The low QFLS pinning for CZTSSe indicates midgap states act as recombination centers, which are detrimental to the photocathode. The increased QFLS pinning for ACZTSSe evidence that Ag-partial substitution vanquishes the Cu_{zn}-related defects, decreasing recombination, enhancing the charge carriers transport, and consequently, improving the hydrogen production.

1. Introduction

Kesterites $Cu_2ZnSn(S,Se)_4$ (CZTSSe) are promising earth-abundant element-based alternatives to the existing chalcogenide absorber thin-film technologies [1–4]. CZTSSe-based solar cells have improved during the past decade until to reach a record efficiency of 12.6% in 2013 [5]. Because of this distinguished performance in the field of photovoltaics, they have been implemented in photoelectrochemical devices for water splitting. Photocathodes have been fabricated with the same configuration as a solar cell, with photocurrents for hydrogen production comparable to short-circuit current (J_{sc}) values obtained from a photovoltaic device. Ros and coworkers. showed that the J_{sc} of the photovoltaic device Mo/CZTSe/CdS/i-ZnO/ITO/TiO_2 and the photocurrent (J_{ph}) produced by water reduction on the photocathode Mo/CZTSe/CdS/i-ZnO/ITO/TiO_2/Pt were similar, equal to approximately 30 mA cm^{-2} [6]. Although the high short-circuit current values, CZTSSe devices suffer from low open-circuit voltage (V_{oc}) associated with the high density of defects due to the multielement composition nature of the quaternary CZTSSe phase [2,7]. This drawback is not limited to photovoltaic devices, in which this disorder also causes a decrease in the onset potential of photocathodes, consequently decreasing the solar-to-hydrogen (STH) conversion efficiency. The high density of available states inside the band gap near the band edges originates a band tail [1,8] attributed to the phenomenon called Cu/Zn disordering [9,10]. Because of their similar ionic radii and comparable valences, Cu^+ and Zn^{2+} leads to a local disorder with a low enthalpic cost for the site exchange, creating Cu/Zn-based bulk defects [11,12]. The Cu_{Zn} and Zn_{Cu} defects identified by Raman spectroscopy led to an onset potential below 0.35 V *versus* the reversible hydrogen electrode (RHE). The annihilation of defects can result in more positive onset potentials, and consequently, may increase the STH conversion efficiency.

Bulk defects can be mitigated by isovalent cation substitution in CZTSSe [12–14]. It can increase the energetic barrier to I-II site exchange and increase the dielectric constant in the absorber layer reducing the charge defects, and consequently, the band tailing [15]. In addition, cations with different sizes from Cu and Zn (ionic radii Cu = Zn = 0.74 Å) can improve ordering [2,15,16]. The partial substitution of Cu^+ by Ag^+ in Cu_2ZnSnS_2 (CZTS) has been successfully demonstrated to enhance onset potential due to the annihilation of the Cu_{Zn} and Zn_{Cu}

* Corresponding author.
E-mail address: lmascaro@ufscar.com (L.H. Mascaro).

https://doi.org/10.1016/j.electacta.2023.142935
Received 4 December 2022; Received in revised form 17 July 2023; Accepted 22 July 2023
Available online 23 July 2023

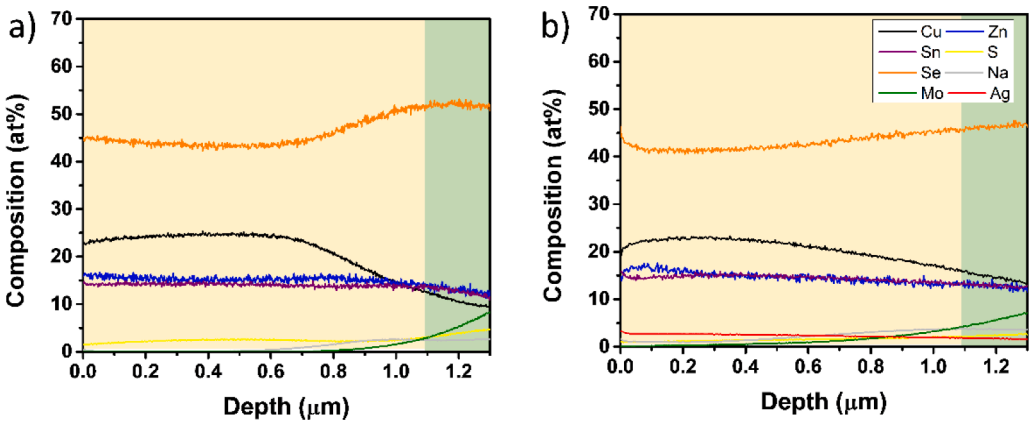

Fig. 1. The elemental profile obtained by GDOES of (a) CTZSSe and (b) ACTZSSe films.

antisites. By substituting until 10% of Cu^{+} by Ag^{+}, the onset potential has increased up to 0.85 V_{RHE}, resulting in an increment of 10 mA cm^{-2} in the photocurrent, and a maximum EQE higher than 80% [17].

Hillhouse group has shown the relation between the open-circuit voltage (V_{oc}) of chalcogenide solar cells and the quasi-Fermi level splitting (QFLS) values obtained from absolute intensity photoluminescence (AIPL) [18,19]. QFLS is estimated by fitting the Katahara-modified LSW photoluminescence model to the room temperature PL spectrum [18]. Gunawan and coworkers have demonstrated that the Fermi level pinning in the curve of light intensity *vs* V_{oc} is caused by the high density of bulk defects in CZTSSe [20].

Here, we demonstrate that the partial substitution of Cu with Ag in CZTSSe promotes an enhancement on the photoelectrochemical activity. The photoelectrochemical results was compared to the characterization of the CZTSSe films by photoluminescence to demonstrate the decrease in the Cu/Zn-related defects with the Ag-substitution. Therefore, by plotting the QFLS as a function of the light intensity, we demonstrate that vanquishing the Cu/Zn-related deep defects by Ag-substitution promotes enlargement of the quasi-Fermi level pinning in comparison with pristine CZTSSe. This method would allow the screening of a variety of candidates CZTSSe films with different cation substitutions and diverse fabrication approaches before the photoelectrochemical application and help to achieve more efficient photocathodes.

2. Experimental

2.1. Molecular precursor solutions

The molecular precursor solutions were prepared based on the method described by Colllord and Hillhouse[21]. Briefly, the CZTSSe precursor solution was prepared by sequentially dissolving 5 mol L^{-1} thiourea TU (99%), 0.48 mol L^{-1} $Cu(CH_3CO_2H)_2$ (99.99%), 0.37 mol L^{-1} $ZnCl_2$ (99.99%), 0.35 mol L^{-1} $SnCl_2$ (99.99%), and 0.03 mol L^{-1} LiCl in dimethylformamide, DMF(99.98%). Elemental ratios were Cu/(Zn+Sn) = 0.75 and Zn/Sn = 1.05 to obtain a Cu-poor and Zn-rich CZTSSe composition. The Ag alloyed CZTSSe (I_2-II-IV-VI_4) precursor solution was prepared by the same procedure described above, adding 0.05 mol L^{-1} AgCl (99.99%) to obtain a film with the composition of $(Cu_{0.9},Ag_{0.1})_2$ Zn Sn(S,Se)$_4$.

2.2. CZTSSe and ACZTSSe film depositions and devices fabrication

The chalcogenide films were deposited onto Mo-coated soda lime glass (MSLG) substrates 2.5 × 2.5 cm, which were cleaned sequentially in deionized water, acetone, and 2-propanol, under sonication, and dried with N_2.

The precursor solutions were filtered using a 0.45 μm PTFE filter and spin-coated onto MSLG substrate at 3000 rpm for 1 min. The films were annealed on a hot plate at 300 °C for 90 s and then allowed to cool. The spin coating and annealing procedures were repeated six times to obtain a film thickness equal to approximately 1200 nm.

The as deposited CZTSSe films were selenized at 520 °C for 20 min under Ar flow of 100 cm^3 min^{-1}.

The CdS buffer layer with a thickness of 40 nm was deposited by chemical bath deposition (CBD) technique[22]. The substrates were immersed in a solution containing 150 ml of deionized water, 22 ml of 0.015 mol L^{-1} $CdSO_4$ solution, 22 mL of 0.75 mol L^{-1} thiourea solution, and 28 ml of NH_4OH at 65 °C for 10 min. At the end, the electrodes were rinsed with ultrapure water and dried under N_2.

The electron transport layer of TiO_2 was deposited over the CdS/CZTSSe by spin coating. The precursor solution was comprised of 20% of titanium isopropoxide in isopropanol, in which 400 µl was necessary to achieve the desired thickness. The electrodes were spun at 3000 rpm for 1 min, and the films were annealed at 200 °C for 30 min afterward.

Finally, a Pt cocatalyst layer was photoelectrodeposited at 0 V *vs* Ag/AgCl under 100 mW cm^{-2} for 30 s. The photoelectrodeposition was carried out in a three-electrode cell, where TiO_2/CdS/CTZSSe/Mo was the working electrode with Pt and Ag/AgCl as the counter and reference electrodes, respectively, in an aqueous solution of 10 µM H_2PtCl_6.

2.3. Film characterization and photoelectrochemical activity

The electrode surface was analyzed by scanning electron microscopy (SEM) technique with FEI Sirion XL30 microscope using a 5 kV accelerating voltage. Energy-dispersive X-ray spectroscopy (EDX) data were collected with an Oxford EDX detector using an accelerating voltage of 20 kV to verify the elemental composition. The X-ray diffraction (XRD) was performed with Cu Kα radiation (40 kV, 30 mA) using a Shimadzu model XRD 6000 diffractometer with 0.5, 0.5, 0.3 mm slits for entrance, scattering, and exit, respectively, at room temperature. The UV–Vis spectra of the chalcogenide films were obtained between 400 and 1400 nm using a Cary5G Varian UV–Vis-NIR spectrophotometer.

The AIPL was collected using a calibrated confocal PL instrument Horiba. The samples were excited with a 785 nm diode, and the emitted light was passed to an InGaAs detector. The band gap (E_g) and the QFLS were calculated by fitting the LSW photoluminescence model modified by Katahara (supplementary information).

Photoelectrochemical measurements were performed using a conventional three-electrode cell with a Pt, Ag/AgCl, and CZTSSe or ACZTSSe as the counter, reference, and working electrodes, respectively. Measurements were conducted by linear sweep voltammetry at 10 mV s^{-1} using 0.5 mol L^{-1} H_2SO_4 solution, deaerated with N_2 gas for 15 min, under 100 mW cm^{-2} chopped sunlight simulated illumination (AM 1.5G) using a solar simulator LCS-100 (Oriel, Newport) equipped with a 100 W Xe lamp as the light source.

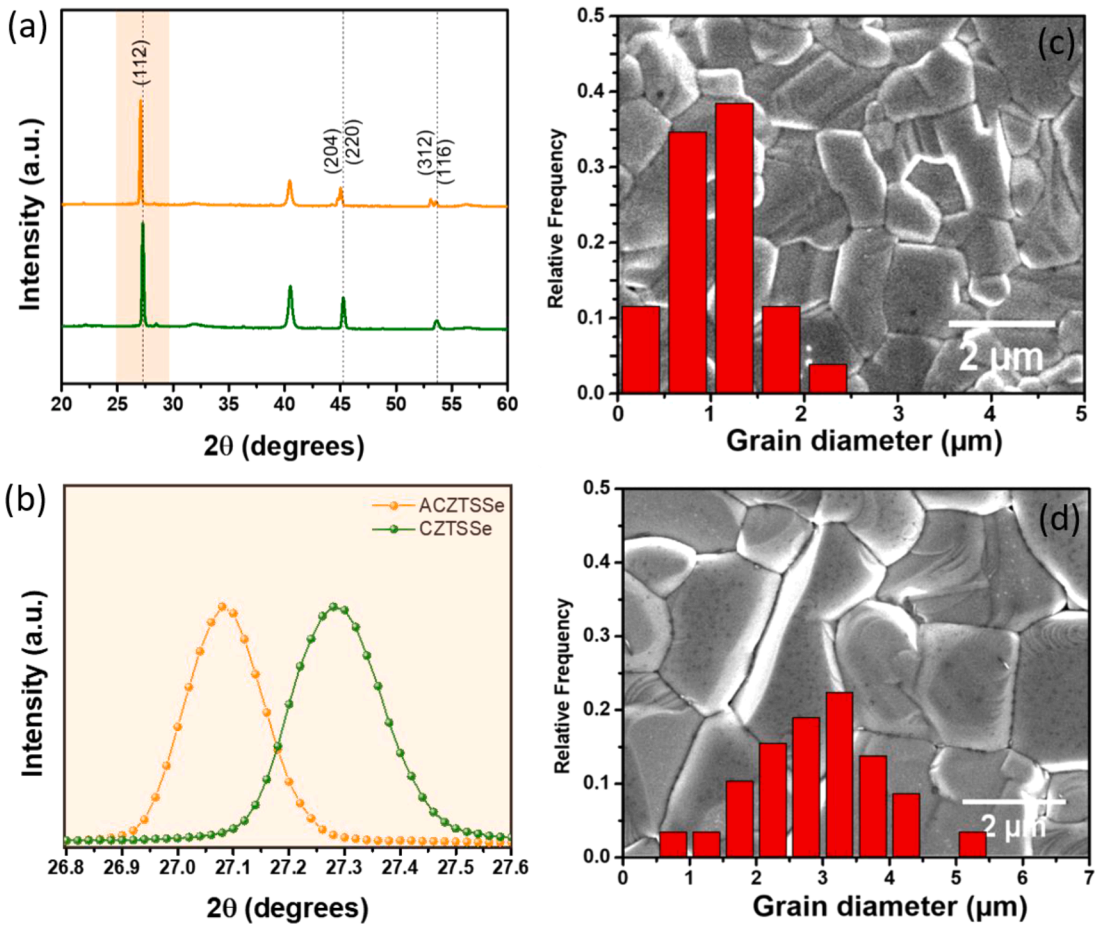

Fig. 2. (a) XRD patterns of CTZSSe and ACTZSSe films and (b) magnified view of XRD spectra of the CZTSSe and ACZTSSe films to verify the shift in peak position at 2θ of 26.8°−27.6° Size distributions of grains in (c) CZTSSe and (d) ACTZSSe films were obtained by measuring the major diameter of all grains in 100 μm x 100 μm images. Insets: Top-view SEM images.

3. Results and discussion

3.1. Characterization of Ag-alloyed CZTSSe films

Fig. 1a and b shows the elemental distribution profile along the CZTSSe and ACZTSSe thickness obtained by glow-discharge optical emission spectrometry (GDOES), respectively. Notably, the composition of CZTSSe and ACZTSSe does not change significantly across the thickness of the films. Furthermore, the increase of Se and Mo intensities for depth bigger than 0.8 μm indicates, as expected, the formation of $MoSe_2$ in the interface (A)CZTS/Mo. Also, as the increment of Zn intensity is not an evident close region of the interface (A)CZTS/Mo, it can be suggested that there is no formation of ZnSe in the interface. The segregation of ZnSe or ZnS in CZTS films has been reported in the literature [23,24].

All the films were prepared under Cu-poor, I/(II+IV) = 0.75, and Zn-rich, II/IV = 1.05, conditions. These ratios prevent the formation of low bandgap ternary phases, such as Cu_2SnS_3, which are favored in Cu-rich compositions [25]. The elemental analysis shows that Cu-poor condition is maintained throughout all compositions with I/(II+IV) approximately 0.75 (Figure S1a). Although II/IV elemental ratio varied between 1.06 and 1.19 (Figure S1b), all the samples are also Zn-rich. The S/(S+Se) ratio is approximately 5% for both films (Figure S1c). For the Ag substituted film Ag/(Ag+Cu) is equal to 10% (Figure S1d).

Fig. 2a shows the XRD pattern of the CZTSSe and ACZTSSe samples which agrees well with the tetragonal kesterite structure (JCPDS No. 96-722-0527) [26–29]. The peak positions in the Ag-substituted film are shifted to lower 2θ angles in comparison with the non-modified CZTSSe structure, as shown by the magnified view of (112) reflections in Fig. 2b. Since the ionic radius of Ag^+ (1.15 Å) is larger than that of Cu^+ (0.74 Å), the observed shifts are strong evidence of the partial Cu replacement to form Ag-substituted kesterite crystals instead of the formation of separate phases [30]. It should be noted that the absence of diffraction peaks other than those for the CZTSSe phase indicates that no significant impurity phases were identified by XRD. The presence of ZnSe secondary phase is quite difficult to be identified by XRD once ZnSe diffraction peaks overlap CZTSSe main peaks [24]. $SnSe_x$ impurity phases are expected in the Cu-poor and Zn-rich film compositions, however, diffraction peaks attributed to these phases are challenging to be detected once they can present very low intensity due to small concentration [31,32]. Impurity phases derivatives from the substituent transition metals, such as Ag_2Se, and Ag_8SnSe_6, reported in the literature for $Ag_2ZnSnSe_4$ [33, 34], have not been detected in the Ag alloyed CZTSSe films. The diffraction peaks at 42° and 33° are related to the Mo substrate and the formation of $MoSe_2$ layer during selenization, respectively [35,36].

Fig. 2c and d show the analyses of grain-size distributions and the top-view SEM images of CZTSSe and ACZTSSe films, respectively. The surface images revealed that both films were composed of densely packed crystal grains without void formation. Based on the analyses of grain-size distributions, it is possible to verify that the partial Cu-replacement with Ag promoted a threefold increased grain size (Fig. 2d) in comparison with the non-modified CZTSSe (Fig. 2c). Ag-induced grain growth has been reported by Huang and co-workers [34]. According to the authors, during selenization, low melting point compounds, such as Sn-Ag-Cu alloy and Ag-related chalcogenides are formed, which induces liquid-assisted grain growth.

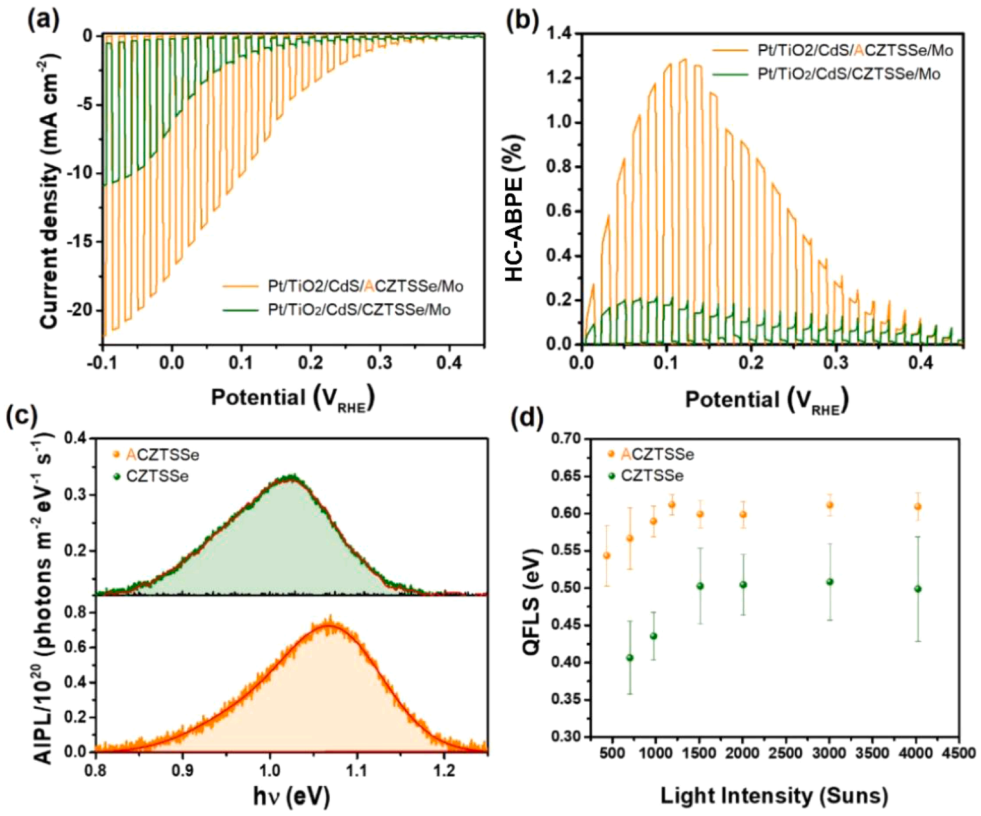

Fig. 3. (a) Current density–potential curves of Pt/TiO_2/CdS/ACZTS and Pt/TiO_2/CdS/CZTS in a 1.0 mol L^{-1} H_2SO_4 solution (pH 0.4) under chopped simulated sunlight (1.5G filter and 100 mW cm^{-2}) and the correspondent (b) Half-cell solar to hydrogen efficiency.

3.2. Solar-driven water splitting on Ag-substituted CZTSSe-based photocathodes

Fig. 3a shows the current-density potential curves for the prepared photocathodes in 0.5 mol L^{-1} H_2SO_4 solution under chopped simulated sunlight. The Pt/TiO_2/CdS/CZTSSe photocathode exhibited a photocurrent density of −6.2 mA cm^{-2} at 0 V_{RHE} and an onset potential of 0.22 V_{RHE}. The partial Cu^+ substitution by Ag^+ promoted a significant improvement in the onset potential (V_{on} ~0.4 V_{RHE}) with high photocurrent density (J_{ph} = −16 mA cm^{-2} at 0 V_{RHE}). The observed onset potential increase can be attributed to the reduction of the deep effects concentration [14,37,38]. Furthermore, the increased photocurrent observed for Pt/TiO_2/CdS/ACZTSSe can be explained by the improved grain morphology (Fig. 2d). The Ag cation incorporation causes the laterally expanding of the grain along the depth direction, which can enhance both the light absorption and carrier collection [34].

Fig. 3b presents the half-cell applied bias photon-to-current efficiency (HC-ABPE) efficiency plot obtained according to Eq. (1).

$$HC-ABPE(\%) = \frac{J_{PH} \times \left(V - V_{H^2/H^+}\right) \times 100\%}{P_{total}} \quad (1)$$

Therefore, the HC-ABPE efficiency for Pt/TiO_2/CdS/ACZTSSe photocathode (1.27%) was more than six times higher than that for the CZTSSe photocathode (0.20%).

To promote a better understanding of the positive effect of the partial Cu^+ substitution by Ag^+ on the radiative recombination pathway, AIPL analysis was performed. Through the model of photoluminescence proposed by Katahara and Hillhouse [18] applied to semiconductors with direct gap absorption coefficients, the AIPL spectra were fitted to calculate the values of the direct bandgap (E_g) and the QFLS. The fully fitted AIPL spectra acquired with an excitation of 785 nm for CZTSSe and ACZTSSe can be seen in Fig. 3c. The E_g values obtained from the fit for both films are commensurate with those extracted from the Tauc plot (Figure S2b). Ag alloying caused an increase of approximately 100 meV in the bandgap (Table 1). The bandgap variation with Ag alloying can be attributed to the valence band maximum (VBM) change due to the antibonding component of the p-d hybridization between Se^{2-}(S^{2-}) and Cu^+(Ag^+) [14].

Table 1
E_g and E_u of the absorbers obtained from UV–Vis-NIR spectroscopy, and the parameters obtained from the AIPL of the CZTSSe and ACZTSSe films by LSWK plotting model.

Absorber	Optical E_g (eV)	E_u (meV)	PL E_g (eV)	QFLS (eV)
CZTSSe	1.03	29.8	1.01	0.469
ACZTSSe	1.11	18.5	1.10	0.627

Under irradiation, the density of the electron-hole generation is related to the amplitude of the quasi-Fermi level splitting (QFLS) [39]. The QFLS determined by fitting the AIPL data is shown in Table 1, and the values for CZTSSe and ACZTSSe were 0.469 eV and 0.627 eV, respectively. Since the ACZTSSe showed a higher value for the QFLS it is possible to infer that the Ag alloying promoted a decrease in the band-tailing states which, in turn, caused an onset potential shift to more positive values in the ACZTS film.

The Urbach tail energy (E_u) was extracted by the inverse of the slope from the linear region below E_g from the plot ln(α) *versus* photon energy (Figure S2) [40]. The results reveal that the E_u decreases with Ag-substitution. The Urbach tail energy for the CZTSSe film was equal to 29.8 meV. This high E_u value above the k_BT is associated with the large density of I-II defects which leads to the band tailing, consequently causing a cathodic shift in the onset potential. On the other hand, the lower E_u value of 18.5 meV associated with the ACZTSSe film indicates a decrease in the antisites defects and a favorable anodic shift in the onset potential.

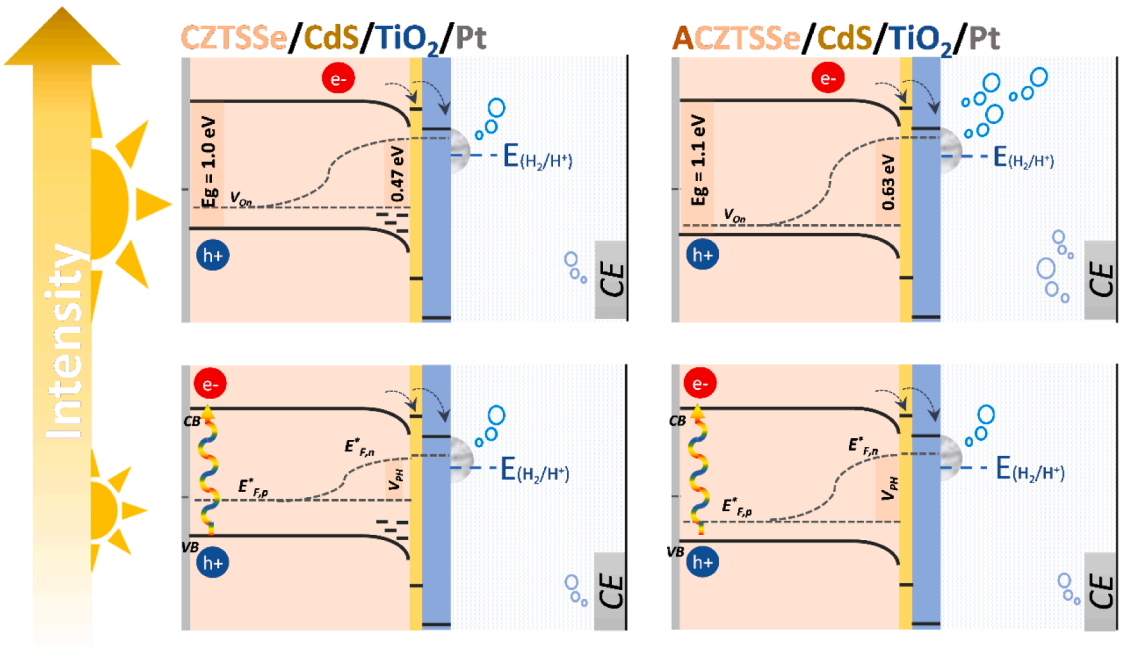

Fig. 4. Scheme representing the increased QFLS as Ag partially substitutes Cu sites in CZTSSe films and with increasing the light intensity, which leads to increased hydrogen production and a more positive onset potential for Pt/TiO_2/CdS/ACZTSSe/Mo photocathodes.

Bulk defects, including band tailing, introduce extra states in the bandgap that could pin the Fermi level [20]. Light intensity *vs* V_{oc} measurements is often used to determine the Fermi level pinning in photovoltaic devices [41]. Similarly, here, AIPL spectra were acquired in different light intensities. The QFLS of each spectrum was determined by fitting the model, and QFLS *vs* light intensity plot is shown in Fig. 3d. The curves showed that QFLS increased with light intensity until 1000 Suns, and then, they were pinned in high intensities. The QFLS pinning for CZTSSe occurred in approximately 0.47 eV, meanwhile, for the Ag-alloyed CZTSSe the QFLS pinned in approximately 0.63 eV. The low QFLS pinning for CZTSSe indicates the presence of mid-gap states from defects and band tailing, as already identified from the E_u values. With increasing irradiation intensity, the quasi-Fermi level splitting proceeds until the population of defects becomes efficient recombination centers inhibiting further quasi-Fermi level to split, consequently, pinning (Fig. 4) [21]. The low efficiency of the CZTSSe photocathode have been assigned to the formation of the band tails and the large rate of recombination of charge carriers caused by Cu/Zn antisites which originates due to the close ionic size of Cu^+ and Zn^{2+}.

The large value of the QFLS pinning for ACZTSSe confirms that Ag-alloying vanquishes the deep defects. The QFLS pinning for ACZTSSe is approximately 150 meV larger than that for CZTSSe, which corresponds to the same value for the onset potential shift for the ACZTSSe photocathodes. This indicates a direct relationship between the QFLS and the onset potential. The larger ionic size of Ag^+ (1.05 Å) than Cu^+ and Zn^{2+} (0.74 Å) avoids the Cu/Zn antisites defects and, consequently, promotes the decrease in the charge carrier recombination and band tail states. Therefore, the evident enhancement of the photoelectrochemical performance of Pt/TiO_2/CdS/ACZTSSe is directly related to the partial Cu^+ substitution by Ag^+ in the CZTSSe film.

4. Conclusions

In summary, the Cu^+ substitution by Ag^+ in the CZTSSe photocathodes was carried out. The substitution was demonstrated by the peaks shifts in the XRD diffractogram. In addition, the SEM micrographs show a grain size increase in the ACZTSSe when compared with the CZTSSe. As a result of the Ag-partial substitution, the Pt/TiO_2/CdS/ACZTSSe photocathode presents a six times higher STH efficiency than that was observed for the CTZSSe. The band-tailing states decrease in the ACZTSSe was demonstrated by AIPL analysis, in which the determined QFLS values were 0.627 eV for the ACZTSSe, in comparison with only 0,469 eV for CZTSSe. In addition, the reduction in the Cu_{Zn} antisites defects was shown in the ACZTSSe photocathode by the lower E_u value equal to 18.5 meV, in comparison with 28.9 meV for the CZTSSe film. Most importantly, the vanquish of the deep defects in the ACZTSSe photocathode was well supported by the value of the QFLS, which was approximately 150 meV larger than that for CZTSSe photocathodes. The findings in the present work provide additional insights into the Cu+ substitution by Ag+ to vanquish the Cu_{Zn}-related defects as a strategy to improve the charge carrier transport in addition to decreasing the recombination. This method has been proposed as a good alternative to preparing CZTSSe thin film with an improved performance to hydrogen production.

CRediT authorship contribution statement

Mileny dos Santos Araujo: Investigation, Methodology, Data curation. **Hugo Leandro Sousa dos Santos:** Investigation, Methodology, Data curation, Writing – original draft, Writing – review & editing. **Marina Medina:** Investigation, Methodology, Data curation, Writing – original draft, Writing – review & editing. **Arthur Corrado Salomao:** Investigation, Methodology, Data curation. **Lucia Helena Mascaro:** Visualization, Supervision, Writing – review & editing, Resources. **Marcos Antonio Santana Andrade:** Investigation, Methodology, Data curation, Visualization, Writing – review & editing.

Declaration of Competing Interest

The authors declare that they have no known competing financial interests or personal relationships that could have appeared to influence the work reported in this paper.

Acknowledgments

The authors acknowledge Fundação de Amparo à Pesquisa no Estado de São Paulo (FAPESP), for A.C.S. (#2020/09000-7), M.A.S.A.J. (#2017/15144-9), H.L.S.S. (#2019/26860-2), M.M. (#2017/12794-2)

fellowships, and for the grants FAPESP/CDMF (#2013/07296-2) and FAPESP/GSK (#2014/50249-8), FAPESP/SHELL (#2017/11986-5). The authors also thanks CNPq/PIBIT for the fellowship to M.S.A. (#116077/2020-4), and Shell and the strategic importance of the support given by ANP (Brazil's National Oil, Natural Gas and Biofuels Agency) through the R&D levy regulation.

Supplementary materials

Supplementary material associated with this article can be found, in the online version, at doi:10.1016/j.electacta.2023.142935.

References

[1] G. Rey, G. Larramona, S. Bourdais, C. Choné, B. Delatouche, A. Jacob, G. Dennler, S. Siebentritt, On the origin of band-tails in kesterite, Sol. Energy Mater. Sol. Cells 179 (2018) 142–151, https://doi.org/10.1016/j.solmat.2017.11.005.

[2] T. Gershon, Y.S. Lee, P. Antunez, R. Mankad, S. Singh, D. Bishop, O. Gunawan, M. Hopstaken, R. Haight, Photovoltaic materials and devices based on the alloyed kesterite absorber (AgxCu1-x)2ZnSnSe4, Adv. Energy Mater. 6 (2016) 1–7, https://doi.org/10.1002/aenm.201502468.

[3] P. Bais, M.T. Caldes, M. Paris, C. Guillot-Deudon, P. Fertey, B. Domengès, A. Lafond, Cationic and anionic disorder in CZTSSe Kesterite compounds: a chemical crystallography study, Inorg. Chem. 56 (2017) 11779–11786, https://doi.org/10.1021/acs.inorgchem.7b01791.

[4] S.K. Wallace, D.B. Mitzi, A. Walsh, The steady rise of kesterite solar cells, ACS Energy Lett. 2 (2017) 776–779, https://doi.org/10.1021/acsenergylett.7b00131.

[5] T. Gokmen, O. Gunawan, D.B. Mitzi, Semi-empirical device model for Cu2ZnSn(S, Se)4 solar cells, Appl. Phys. Lett. 105 (2014) 2–7, https://doi.org/10.1063/1.4890844.

[6] C. Ros, T. Andreu, S. Giraldo, V. Izquierdo-Roca, E. Saucedo, J.R. Morante, Turning earth abundant kesterite-based solar cells into efficient protected water-splitting photocathodes, ACS Appl. Mater. Interfaces 10 (2018) 13425–13433, https://doi.org/10.1021/acsami.8b00062.

[7] M. Dimitrievska, F. Oliva, M. Guc, S. Giraldo, E. Saucedo, A. Pérez-Rodríguez, V. Izquierdo-Roca, Defect characterisation in Cu2ZnSnSe4 kesterites: via resonance Raman spectroscopy and the impact on optoelectronic solar cell properties, J. Mater. Chem. A. 7 (2019) 13293–13304, https://doi.org/10.1039/c9ta03625c.

[8] Y.F. Tay, H. Kaneko, S.Y. Chiam, S. Lie, Q. Zheng, B. Wu, S.S. Hadke, Z. Su, P. S. Bassi, D. Bishop, T.C. Sum, T. Minegishi, J. Barber, K. Domen, L.H. Wong, Solution-processed Cd-substituted CZTS photocathode for efficient solar hydrogen evolution from neutral water, Joule 2 (2018) 537–548, https://doi.org/10.1016/j.joule.2018.01.012.

[9] J. Li, D. Wang, X. Li, Y. Zeng, Y. Zhang, Cation substitution in earth-abundant kesterite photovoltaic materials, Adv. Sci. 5 (2018), https://doi.org/10.1002/advs.201700744.

[10] D. Shin, B. Saparov, D.B. Mitzi, Defect engineering in multinary earth-abundant chalcogenide photovoltaic materials, Adv. Energy Mater. (2017), https://doi.org/10.1002/aenm.201602366.

[11] M. Neuschitzer, Y. Sanchez, T. Olar, T. Thersleff, S. Lopez-Marino, F. Oliva, M. Espindola-Rodriguez, H. Xie, M. Placidi, V. Izquierdo-Roca, I. Lauermann, K. Leifer, A. Pérez-Rodriguez, E. Saucedo, Complex surface chemistry of kesterites: Cu/Zn reordering after low temperature postdeposition annealing and its role in high performance devices, Chem. Mater. 27 (2015) 5279–5287, https://doi.org/10.1021/acs.chemmater.5b01473.

[12] S. Lie, J.M.R. Tan, W. Li, S.W. Leow, Y.F. Tay, D.M. Bishop, O. Gunawan, L. H. Wong, Reducing the interfacial defect density of CZTSSe solar cells by Mn substitution, J. Mater. Chem. A 6 (2018) 1540–1550, https://doi.org/10.1039/c7ta09668b.

[13] D.B. Khadka, S.Y. Kim, J.H. Kim, Effects of Ge alloying on device characteristics of kesterite-based CZTSSe thin film solar cells, J. Phys. Chem. C. 120 (2016) 4251–4258, https://doi.org/10.1021/acs.jpcc.5b11594.

[14] Y. Qi, Q. Tian, Y. Meng, D. Kou, Z. Zhou, W. Zhou, S. Wu, Elemental precursor solution processed (Cu1-xAgx)2ZnSn(S,Se)4 photovoltaic devices with over 10% efficiency, ACS Appl. Mater. Interfaces 9 (2017) 21243–21250, https://doi.org/10.1021/acsami.7b03944.

[15] T. Gershon, D. Bishop, P. Antunez, S. Singh, K.W. Brew, Y.S. Lee, O. Gunawan, T. Gokmen, T. Todorov, R. Haight, Unconventional kesterites: the quest to reduce band tailing in CZTSSe, Curr. Opin. Green Sustain. Chem. 4 (2017) 29–36, https://doi.org/10.1016/j.cogsc.2017.01.003.

[16] X. Li, Z. Hou, S. Gao, Y. Zeng, J. Ao, Z. Zhou, B. Da, W. Liu, Y. Sun, Y. Zhang, Efficient optimization of the performance of Mn2+-doped kesterite solar cell: machine learning aided synthesis of high efficient Cu2(Mn,Zn)Sn(S,Se)4 solar cells, Sol. RRL 2 (2018) 1–8, https://doi.org/10.1002/solr.201800198.

[17] Y.F. Tay, S.S. Hadke, M. Zhang, N. Lim, S.Y. Chiam, L.H. Wong, Improving the interfacial properties of CZTS photocathodes by Ag substitution, J. Mater. Chem. A 8 (2020) 8862–8867, https://doi.org/10.1039/d0ta02042g.

[18] J.K. Katahara, H.W. Hillhouse, Quasi-fermi level splitting and sub-bandgap absorptivity from semiconductor photoluminescence, J. Appl. Phys. 116 (2014), https://doi.org/10.1063/1.4898346.

[19] A.R. Uhl, J.K. Katahara, H.W. Hillhouse, Molecular-ink route to 13.0% efficient low-bandgap CuIn(S,Se)2and 14.7% efficient Cu(In,Ga)(S,Se)2 solar cells, Energy Environ. Sci. 9 (2016) 130–134, https://doi.org/10.1039/c5ee02870a.

[20] O. Gunawan, T. Gokmen, D.B. Mitzi, Suns-VOC characteristics of high performance kesterite solar cells, J. Appl. Phys. 116 (2014), https://doi.org/10.1063/1.4893315.

[21] A.D. Collord, H.W. Hillhouse, Germanium alloyed kesterite solar cells with low voltage deficits, Chem. Mater. 28 (2016) 2067–2073, https://doi.org/10.1021/acs.chemmater.5b04806.

[22] Q. Guo, S.J. Kim, M. Kar, W.N. Shafarman, R.W. Birkmire, E.A. Stach, R. Agrawal, H.W. Hillhouse, Development of CulnSe 2 nanocrystal and nanoring inks for low-cost solar cells, Nano Lett. 8 (2008) 2982–2987, https://doi.org/10.1021/nl802042g.

[23] M.I. Khalil, O. Atici, A. Lucotti, S. Binetti, A. Le Donne, L. Magagnin, CZTS absorber layer for thin film solar cells from electrodeposited metallic stacked precursors (Zn/Cu-Sn), Appl. Surf. Sci. 379 (2016) 91–97, https://doi.org/10.1016/j.apsusc.2016.04.062.

[24] J. Just, C.M. Sutter-Fella, D. Lützenkirchen-Hecht, R. Frahm, S. Schorr, T. Unold, Secondary phases and their influence on the composition of the kesterite phase in CZTS and CZTSe thin films, Phys. Chem. Chem. Phys. 18 (2016) 15988–15994, https://doi.org/10.1039/c6cp00178e.

[25] C.J. Bosson, M.T. Birch, D.P. Halliday, K.S. Knight, A.S. Gibbs, P.D. Hatton, Cation disorder and phase transitions in the structurally complex solar cell material Cu2ZnSnS4, J. Mater. Chem. A. 5 (2017) 16672–16680, https://doi.org/10.1039/c7ta03603e.

[26] J. Li, S.Y. Kim, D. Nam, X. Liu, J.H. Kim, H. Cheong, W. Liu, H. Li, Y. Sun, Y. Zhang, Tailoring the defects and carrier density for beyond 10% efficient CZTSe thin film solar cells, Sol. Energy Mater. Sol. Cells 159 (2017) 447–455, https://doi.org/10.1016/j.solmat.2016.09.034.

[27] G. Suresh Babu, Y.B. Kishore Kumar, P. Uday Bhaskar, S. Raja Vanjari, Effect of Cu/(Zn+Sn) ratio on the properties of co-evaporated Cu2ZnSnSe4 thin films, Sol. Energy Mater. Sol. Cells 94 (2010) 221–226, https://doi.org/10.1016/j.solmat.2009.09.005.

[28] G.M. Ilari, C.M. Fella, C. Ziegler, A.R. Uhl, Y.E. Romanyuk, A.N. Tiwari, Cu 2ZnSnSe 4 solar cell absorbers spin-coated from amine-containing ether solutions, Sol. Energy Mater. Sol. Cells 104 (2012) 125–130, https://doi.org/10.1016/j.solmat.2012.05.004.

[29] A.V. Stanchik, V.F. Gremenok, R. Juskenas, I.I. Tyukhov, M.S. Tivanov, C. Fettkenhauer, V.V. Shvartsman, R. Giraitis, U. Hagemann, D.C. Lupascu, Effects of selenization time and temperature on the growth of Cu2ZnSnSe4 thin films on a metal substrate for flexible solar cells, Sol. Energy 178 (2019) 142–149, https://doi.org/10.1016/j.solener.2018.12.025.

[30] A.F. Wells, Structural_Inorganic_Chemistry.pdf, (1975).

[31] Y.C. Lin, Z.Y. Su, Tin-selenium secondary phase etching of Cu2ZnSnSe4: a selective removal route to improve solar cell efficiency, ACS Appl. Energy Mater. 1 (2018) 6725–6729, https://doi.org/10.1021/acsaem.8b01598.

[32] M. Dimitrievska, A. Fairbrother, E. Saucedo, A. Pérez-Rodríguez, V. Izquierdo-Roca, Secondary phase and Cu substitutional defect dynamics in kesterite solar cells: impact on optoelectronic properties, Sol. Energy Mater. Sol. Cells 149 (2016) 304–309, https://doi.org/10.1016/j.solmat.2016.01.029.

[33] T. Gershon, K. Sardashti, Y.S. Lee, O. Gunawan, S. Singh, D. Bishop, A.C. Kummel, R. Haight, Compositional effects in Ag2ZnSnSe4 thin films and photovoltaic devices, Acta Mater. 126 (2017) 383–388, https://doi.org/10.1016/j.actamat.2017.01.003.

[34] W.C. Huang, S.Y. Wei, C.H. Cai, W.H. Ho, C.H. Lai, The role of Ag in aqueous solution processed (Ag,Cu) 2 ZnSn(S,Se) 4 kesterite solar cells: antisite defect elimination and importance of Na passivation, J. Mater. Chem. A 6 (2018) 15170–15181, https://doi.org/10.1039/c8ta02950d.

[35] M.H. Sayed, J. Schoneberg, J. Parisi, L. Gütay, Improvement of the structural and electronic properties of CZTSSe solar cells from spray pyrolysis by a CuGe seed layer, RSC Adv. 7 (2017) 20406–20411, https://doi.org/10.1039/c7ra02129a.

[36] L. Yao, J. Ao, M.J. Jeng, J. Bi, S. Gao, G. Sun, Q. He, Z. Zhou, Y. Sun, L.B. Chang, A CZTSe solar cell with 8.2% power conversion efficiency fabricated using electrodeposited Cu/Sn/Zn precursor and a three-step selenization process at low Se pressure, Sol. Energy Mater. Sol. Cells 159 (2017) 318–324, https://doi.org/10.1016/j.solmat.2016.09.028.

[37] J. Márquez, H. Stange, C.J. Hages, N. Schaefer, S. Levcenko, S. Giraldo, E. Saucedo, K. Schwarzburg, D. Abou-Ras, A. Redinger, M. Klaus, C. Genzel, T. Unold, R. Mainz, Chemistry and dynamics of Ge in kesterite: toward band-gap-graded absorbers, Chem. Mater. 29 (2017) 9399–9406, https://doi.org/10.1021/acs.chemmater.7b03416.

[38] Y.F. Qi, D.X. Kou, W.H. Zhou, Z.J. Zhou, Q.W. Tian, Y.N. Meng, X.S. Liu, Z.L. Du, S. X. Wu, Engineering of interface band bending and defects elimination via a Ag-graded active layer for efficient (Cu,Ag)2ZnSn(S,Se)4 solar cells, Energy Environ. Sci. 10 (2017) 2401–2410, https://doi.org/10.1039/c7ee01405h.

[39] S. Bourdais, C. Choné, B. Delatouche, A. Jacob, G. Larramona, C. Moisan, A. Lafond, F. Donatini, G. Rey, S. Siebentritt, A. Walsh, G. Dennler, Is the Cu/Zn disorder the main culprit for the voltage deficit in kesterite solar cells? Adv. Energy Mater. 6 (2016) 1–21, https://doi.org/10.1002/aenm.201502276.

[40] J. Chantana, Y. Kawano, T. Nishimura, A. Mavlonov, T. Minemoto, Impact of Urbach energy on open-circuit voltage deficit of thin-film solar cells, Sol. Energy Mater. Sol. Cells 210 (2020), 110502, https://doi.org/10.1016/j.solmat.2020.110502.

[41] P. Calado, D. Burkitt, J. Yao, J. Troughton, T.M. Watson, M.J. Carnie, A.M. Telford, B.C. O'Regan, J. Nelson, P.R.F. Barnes, Identifying dominant recombination mechanisms in perovskite solar cells by measuring the transient ideality factor,

Phys. Rev. Appl. 11 (2019) 1, https://doi.org/10.1103/PhysRevApplied.11.044005.